

## Two-dimensional electronic spectroscopy for mapping molecular photophysics\*

Jessica M. Anna, Yin Song, Rayomond Dinshaw, and  
Gregory D. Scholes<sup>‡</sup>

*Department of Chemistry, University of Toronto, 80 St. George St., Toronto,  
Ontario, M5S 3H6, Canada*

**Abstract:** We demonstrate the ability of two-dimensional electronic spectroscopy (2DES) to map ultrafast energy transfer and dynamics in two systems: the pigment–protein complex photosystem I (PSI) and aggregates of the conjugated polymer poly(3-hexylthiophene) (P3HT). A detailed description of our experimental set-up and data processing procedure is also given.

**Keywords:** energy transfer; light harvesting; molecular aggregates; phasing; photosynthesis; two-dimensional electronic spectroscopy; ultrafast spectroscopy.

### INTRODUCTION

Photoexcitation of molecules initiates dynamics leading to photochemical or photophysical transformation. These dynamics are associated with structural changes or fluctuations of the molecules and can often be ultrafast (i.e., arriving on fs or ps timescales). Ideally we would like to elucidate a kind of map of these dynamics that reveals not only the timescales of various transformations and relaxations, but also mechanistic information on the pathways involved. One recent example of research activity in this direction is the investigation of the role quantum coherences play in the mechanism of photosynthesis [1–7]. Despite these recent advances, the question remains, how can the kind of “map” envisioned above be obtained?

The first steps to understanding photoinitiated dynamics generally involves assigning spectral signatures to important reactants, products, and intermediates, then suggesting a kinetic model for how the species interconvert based on the changes of the spectral signatures. There are two weaknesses to this approach. First, in complex condensed phase systems, spectral signatures are often overlapped and therefore obscured. Second, kinetics provide a weak test of the mechanism for a number of reasons. The signal-to-noise ratio required to distinguish between the ability of different kinetic models to reproduce experimental observables is hard to achieve [8,9]. Further complications arise in complex condensed-phase systems where a distribution of rate constants may be more appropriate for describing the system. Standard kinetic experiments lack the ability to distinguish whether this distribution of rate constants is due to environmental factors, where the molecules are in different local solvent environments, or if it should be attributed to the complex electronic structure of the molecule [10,11].

In this article, we will explain how two-dimensional electronic spectroscopy (2DES) elevates some of these issues and therefore provides a useful next step in exploration of photoinitiated dynamics.

---

\**Pure Appl. Chem.* **85**, 1257–1513 (2013). A collection of invited papers based on presentations at the XXIV<sup>th</sup> IUPAC Symposium on Photochemistry, Coimbra, Portugal, 15–20 July 2012.

<sup>‡</sup>Corresponding author

First, we will give a brief introduction to 2DES and a description of our experimental set-up, followed by a detailed description of our data processing procedure. Finally, we demonstrate how 2DES can be used to elucidate ultrafast (0–400 fs timescale) photophysical events in two systems: poly(3-hexylthiophene) (P3HT) and photosystem I (PSI).

## TWO-DIMENSIONAL ELECTRONIC SPECTROSCOPY

A wealth of information on energy-transfer dynamics and electronic structure can be obtained by applying electronic spectroscopy to complex condensed-phase systems. Steady-state measurements such as linear absorption, fluorescence, excitation anisotropy, and circular dichroism can provide information on the electronic structure. Additional information can be obtained by conducting these measurements at cryogenic temperatures to reduce the effects of homogeneous line broadening; however, the distinction between homogeneous and inhomogeneous broadening is still ambiguous [12,13]. Time-resolved methods, such as transient absorption and pump–probe spectroscopies, can be used to gain further insight into electronic structure while also monitoring energy-transfer dynamics [14,15]. However, when using these techniques, one must choose between either high frequency or time resolution.

2DES has emerged as an optical technique that can accomplish many of the objectives of conventional spectroscopies, while overcoming the limitations mentioned above. A 2D spectrum spreads information contained in a 1D pump–probe spectrum over two frequency axis resulting in a frequency–frequency correlation map, where each excitation frequency is correlated to each detection frequency [16,17]. To obtain a 2D spectrum, three femtosecond optical fields,  $E_1$ ,  $E_2$ , and  $E_3$  having wavevectors  $\mathbf{k}_1$ ,  $\mathbf{k}_2$ , and  $\mathbf{k}_3$  interact with the sample leading to the emission of the signal,  $E_s$ . In the most common implementation of 2D optical spectroscopy, the incoming fields are arranged in a box geometry so that the signal is emitted in the background-free direction, and the two relevant phase-matching conditions, referred to as “rephasing” ( $\mathbf{k}_{\text{signal}} = -\mathbf{k}_1 + \mathbf{k}_2 + \mathbf{k}_3$ ) and “nonrephasing” ( $\mathbf{k}_{\text{signal}} = +\mathbf{k}_1 - \mathbf{k}_2 + \mathbf{k}_3$ ), are collected independently. The beam geometry and pulse sequence are displayed in Fig. 1. The first pulse,  $E_1$ , creates a coherent superposition between the ground state and a first excited state of the system effectively labeling the molecules. This superposition state evolves during the coherence time,  $t_1$ . The arrival of the second pulse,  $E_2$ , creates either a population or another coherence, marking the end of  $t_1$  and the beginning of the waiting time,  $t_2$ . The system is free to evolve during the waiting time, which ends with the arrival of the third pulse. The third pulse,  $E_3$ , creates a second coherence that effectively reads out the current state of the previously labeled molecule. This second coherence can be between the ground and the first excited state manifold in the case of stimulated emission and ground-state bleaching or between the first and second excited-state manifold in the case of excited-state absorption. The arrival of the third pulse marks the beginning of the  $t_3$  coherence time period and leads to the emission of the signal,  $E_s$ . The emitted signal is heterodyne detected by overlapping it with a fourth pulse known as the local oscillator,  $E_{\text{LO}}$ , allowing for both phase and amplitude information to be obtained. Fourier transformation with respect to  $t_1$  and  $t_3$  yields the excitation and detection frequency axes,  $\omega_1$ , and  $\omega_3$ , resulting in a 2D spectrum for a given waiting time,  $t_2$ .

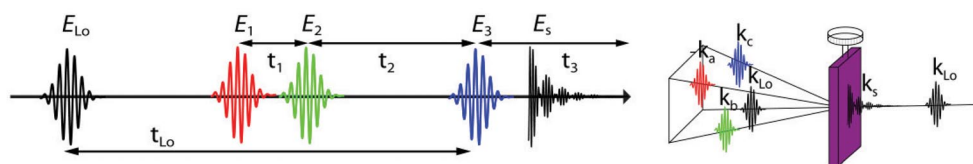


**Fig. 1** The pulse sequence and beam geometry are shown. For rephasing pathways,  $\mathbf{k}_a = \mathbf{k}_1$ ,  $\mathbf{k}_b = \mathbf{k}_2$ , and  $\mathbf{k}_c = \mathbf{k}_3$ ; and for nonrephasing pathways  $\mathbf{k}_a = \mathbf{k}_2$ ,  $\mathbf{k}_b = \mathbf{k}_1$ , and  $\mathbf{k}_c = \mathbf{k}_3$ .

Since each excitation frequency is correlated to each detection frequency, the resulting 2D spectrum contains information on energy transfer pathways—mapping the flow of energy between different spectroscopic signatures. Cross-peaks in the spectrum can result from either electronic coupling and/or energy transfer. Monitoring the waiting-time-dependent growth, decay, and line-shape changes of peaks in the 2D spectrum gives detailed information on the mechanistic pathways and timescales of energy flow in the system [18,19].

### Experimental set-up

The experimental set-up is shown in Fig. 2 and has been described previously [4]. A 5-kHz Ti:sapphire regenerative amplified laser system outputs nearly transform limited 0.6 mJ, 150 fs, pulses centered at 800 nm that pump a home-built noncollinear optical parametric amplifier (NOPA) [20]. The NOPA output is compressed to 10–15 fs via a combination of a grating and single prism compressors [21,22]. The pulse compression is characterized using transient-grating frequency-resolved optical gating (TG-FROG) and methanol as the nonlinear medium [23]. The compressed pulse then enters the four-wave-mixing apparatus. Using a 2D diffractive optic, four identical phase-stable beams in a box geometry are obtained [24]. The four beams are collimated using two 50-cm spherical mirrors that are  $0^\circ$  with respect to each other, this is achieved by using a small steering mirror that reflects the four beams  $90^\circ$  upon exit from the diffractive optic. The four beams then bypass the steering mirror as they pass between the collimating spherical mirrors. Perpendicular to three of the beams are pairs of  $1^\circ$  UV fused silica glass wedges, which when inserted into the beam path can delay the pulse without altering its direction [25]. One glass wedge from each pair is mounted onto a translation stage (Newport VP-25XL), which allows for the  $t_1$  time delay to be controlled with  $\sim 0.9$  as accuracy. The third excitation pulse is chopped at 25 Hz allowing for scatter to be subtracted from the third-order signal. A neutral density filter is inserted

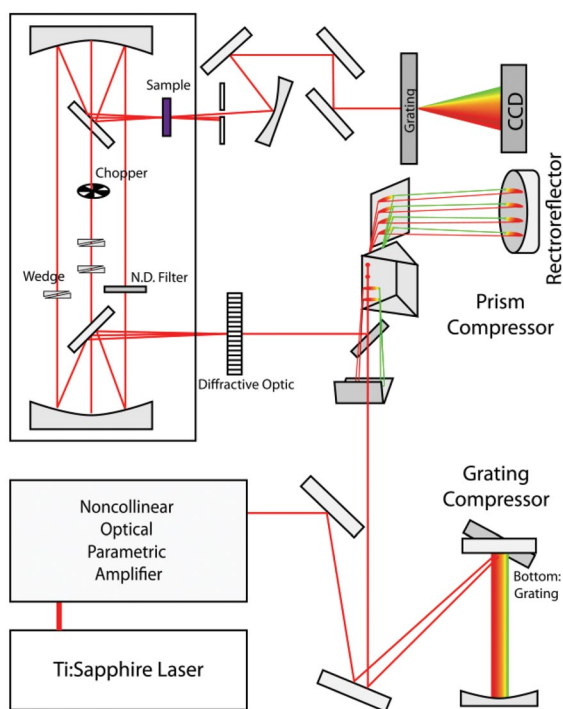


Fig. 2 The experimental set-up is shown. See text for details.

in the path of the fourth beam,  $E_{\text{LO}}$ , which delays the pulse by  $\sim 250$  fs. The three incoming fields, having an approximate energy of 3–10 nJ each, are focused at the sample plane where the beam waist diameter is 50  $\mu\text{m}$ . The signal,  $E_s$ , is emitted in the direction of  $E_{\text{LO}}$ . The signal and local oscillator are collimated using a spherical mirror and directed into the spectrometer where they spectrally interfere on the charge-coupled device (CCD) camera. Auxiliary measurements of the intensity of  $E_{\text{LO}}$  are obtained by blocking  $E_1$ ,  $E_2$ , and  $E_3$  with an automated shutter. Auxiliary pump–probe spectra where  $E_3$  acts as the pump and  $E_{\text{LO}}$  as the probe are obtained by blocking  $E_1$  and  $E_2$ .

## Data processing

The raw data consists of a series of interferograms between  $E_s$  and  $E_{\text{LO}}$  collected for each  $t_1$  step for a given  $t_2$  time. The detected intensity is given by eq. 1 and depends on both the signal field,  $E_s$ , and the local oscillator field,  $E_{\text{LO}}$ , which is delayed by  $\Delta t_{\text{LO}}$  [26–30].

$$I(\omega_3; t_1, t_2) = \left| E_{\text{LO}}(\omega_3) e^{i\omega_3 \Delta t_{\text{LO}}} + E_s(\omega_3; t_1, t_2) \right|^2 = \\ \left| E_{\text{LO}}(\omega_3) \right|^2 + \left| E_s(\omega_3; t_1, t_2) \right|^2 + \\ E_{\text{LO}}(\omega_3) e^{i\omega_3 \Delta t_{\text{LO}}} E_s^*(\omega_3; t_1, t_2) + E_{\text{LO}}^*(\omega_3) e^{-i\omega_3 \Delta t_{\text{LO}}} E_s(\omega_3; t_1, t_2) \quad (1)$$

In the semi-impulsive limit, the last interference term in eq. 1 is proportional to the third-order response of the system. The mathematical operations required to isolate this term are given in eq. 2, where  $F$  and  $F^{-1}$  denote Fourier and inverse Fourier transformation and  $\Theta$  is the Heaviside function [28].

$$S_S(\omega_3; t_1, t_2) \propto E_{\text{LO}}^*(\omega_3) E_S(\omega_3; t_1, t_2) = F \left[ \Theta(t_3) F^{-1} I(\omega_3; t_1, t_2) \right] e^{i\omega_3 \Delta t_{\text{LO}}} \quad (2)$$

From the isolated signal, the 2D spectrum is obtained by performing a Fourier transformation along  $t_1$  and  $t_3$  (where the  $t_3$  Fourier transform is typically performed experimentally by the spectrometer). In the background-free geometry of 2DES, the rephasing and nonrephasing signals are collected separately and the absorptive 2D spectrum is obtained by adding the individually collected rephasing and nonrephasing components (eq. 3) [27,31].

$$S(\omega_1, t_2, \omega_3) = \\ \text{Re} \left[ \int_0^\infty dt_1 \int_0^\infty dt_3 S_R(t_1, t_2, t_3) e^{-i\omega_1 t_1} e^{i\omega_3 t_3} + \int_0^\infty dt_1 \int_0^\infty dt_3 S_{\text{NR}}(t_1, t_2, t_3) e^{i\omega_1 t_1} e^{i\omega_3 t_3} \right] \quad (3)$$

A detailed description on how to obtain absorptive 2D spectra from the raw data of the laser dye Rhodamine 800 (R800) in methanol follows. Figure 3a displays the raw data read from the CCD camera for a given value of  $t_2 = 200$  fs. The data consists of a series of interferograms for each  $t_1$  time where the scatter and the intensity of the local oscillator have already been subtracted. The raw data are frequency resolved along the detection axis and time resolved along the excitation axis. Negative values of  $t_1$  correspond to the nonrephasing signal and positive values to the rephasing signal. The desired interference term (eq. 2) is isolated by first interpolating the wavelength axis to be evenly spaced in frequency, inverse Fourier transforming along  $\omega_3$  to the time domain, and filtering the data to isolate the interference term at positive time delays (Fig. 3b). The filtered data are then Fourier transformed back to the frequency domain where the linear spectral phase is removed (Fig. 3c). The linear spectral phase is obtained from an auxiliary measurement of the spectral interference between the local oscillator and the nonresonant solvent response of methanol (Fig. 3d). Figures 3e and 3f display the absolute value of the rephasing and nonrephasing spectra resulting from Fourier transformation along the interpolated  $t_1$  axis.

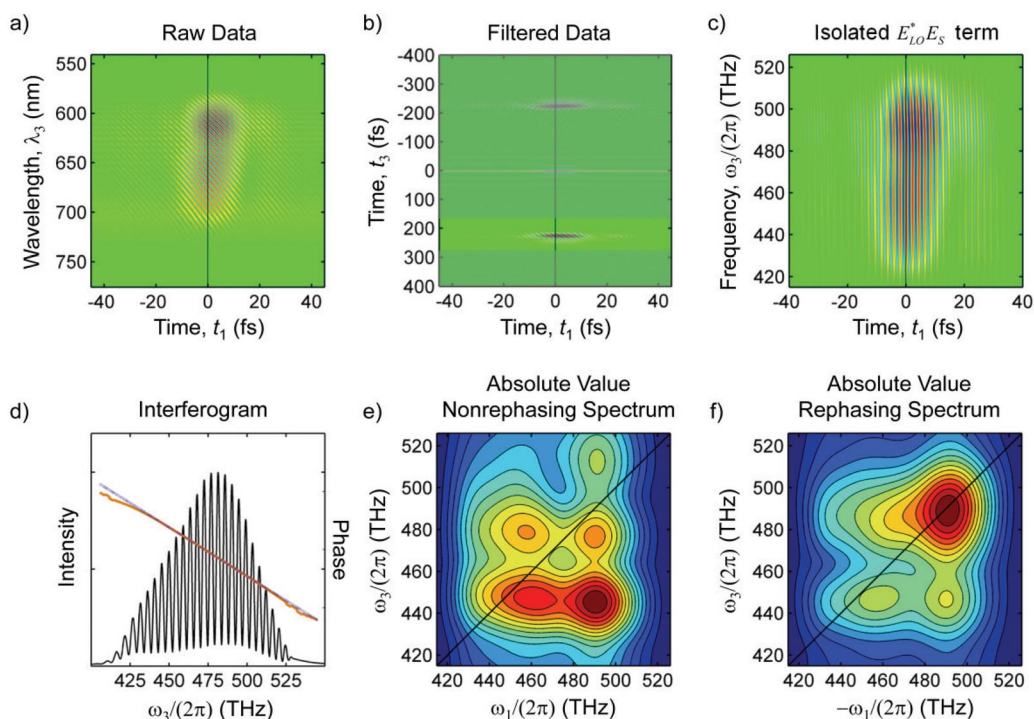


**Fig. 3** The raw data (a) is interpolated to be evenly spaced in frequency. The data is inverse Fourier transformed to the time domain where it is filtered to isolate the desired interference term (b). The data is then Fourier transformed along  $t_3$  back to the frequency domain (c) where the linear spectral phase (d) is removed. Fourier transformation along  $t_1$  yields the excitation axis,  $\omega_1$ , and the resulting nonrephasing (e) and rephasing (f) 2D spectra.

The absorptive spectrum is the sum of the rephasing and nonrephasing spectra (eq. 3). However, errors in the precise origin of the  $t_1$  and  $t_3$  time delays along with the fact that the spectra were collected independently can lead to dispersive contributions in the absorptive spectrum [32–35]. To avoid mixing of real and imaginary parts, the spectra need to be “phased”. Typical phasing procedures call for the 2D spectra to be multiplied by  $\exp(\varphi)$  where  $\varphi_R = i\omega_1\Delta t_{1,R} - i\theta$  for the rephasing spectrum and  $\varphi_{NR} = -i\omega_1\Delta t_{1,NR} - i\theta$  for the nonrephasing spectrum (eq. 4).

$$S(\omega_1, t_2, \omega_3) = \text{Real} \left[ S_R(\omega_1, t_2, \omega_3) e^{(i\omega_1\Delta t_{1,R} - i\theta)} + S_{NR}(\omega_1, t_2, \omega_3) e^{(-i\omega_1\Delta t_{1,NR} - i\theta)} \right] \quad (4)$$

The time delays  $\Delta t_{1,NR}$  and  $\Delta t_{1,R}$  account for inaccuracies in the precise origin of the time delay  $t_1$ , and the constant-phase term arises because the rephasing and nonrephasing spectra were obtained independently by scanning two different wedge pairs. We note that the process of phasing can be circumvented by performing 2D optical spectroscopy in the pump–probe geometry [33,36], or by characterizing the incoming optical fields [34,35]. In some cases, it is sufficient to analyze the absolute value of the spectra, in which case knowledge of the phase is not needed. However, when one is interested in analyzing a system that is spectrally congested or when line-shape analysis is performed, the absolute value of the rephasing or nonrephasing spectrum is not sufficient to extract meaningful information.

To obtain a purely absorptive spectrum, we employ an unconstrained nonlinear optimization procedure to determine the three phase parameters,  $\Delta t_{1,R}$ ,  $\Delta t_{1,NR}$ , and  $\theta$ , that minimize the fitness function,  $f$ , defined in eq. 5, where  $S_{pp}$  is the pump–probe spectrum,  $S_R$  is the rephasing spectrum,  $S_{NR}$  is the nonrephasing spectrum, and  $S$  is defined by eq. 4.

$$\begin{aligned}
 f &= f_{\omega_3} + f_{\omega_1} \\
 f_{\omega_3} &= \sum \left( \left[ S_{\text{PP}}(\omega_3, t_2) - \int S(\omega_1, t_2, \omega_3) d\omega_1 \right]^2 \right) \\
 f_{\omega_1} &= \sum \left( \left| \int S(\omega_1, t_2, \omega_3) d\omega_3 - \int |S_{\text{R}}(\omega_1, t_2, \omega_3)| d\omega_3 \right|^2 \right. \\
 &\quad \left. + \sum \left( \left| \int S(\omega_1, t_2, \omega_3) d\omega_3 - \int |S_{\text{NR}}(\omega_1, t_2, \omega_3)| d\omega_3 \right|^2 \right) \right)
 \end{aligned} \tag{5}$$

The fitness function has two contributions, one along  $\omega_3, f_{\omega_3}$ , and the other along  $\omega_1, f_{\omega_1}$ . For the constraint along  $\omega_3$ , we make use of the projection slice theorem which states that the projection of the real part of the absorptive spectrum onto the  $\omega_3$  axis is equivalent to the pump–probe spectrum obtained under the same experimental conditions [31,32]. For the constraint along the  $\omega_1$  axis, we make use of the fact that the transition frequencies should not be altered by the phase [37,38]. The constraint along  $\omega_1$  is satisfied when the differences between the projection of the absolute value of the real part of the absorptive spectrum and the projection of the absolute value of the rephasing spectrum and absolute value of the nonrephasing spectrum onto the  $\omega_1$  axis are minimized. For small values of  $\Delta t_{1,\text{NR}}$  and  $\Delta t_{1,\text{R}}$ , the linear phase may be approximated as a constant phase [32]:  $\varphi_{\text{R}} = i\omega_1 \Delta t_{1,\text{R}} - i\theta \approx -i\theta_{\text{R}}$  and  $\varphi_{\text{NR}} = -i\omega_1 \Delta t_{1,\text{NR}} - i\theta \approx -i\theta_{\text{NR}}$ ; and the unconstrained nonlinear optimization procedure can be applied to obtain the two phase parameters,  $\theta_{\text{NR}}$  and  $\theta_{\text{R}}$ .

Figure 4 plots the absorptive spectrum of R800 in methanol at  $t_2 = 200$  fs phased with (a) our previous method of phasing [4] and with the method described above when (b) two phase parameters,  $\theta_{\text{NR}}$  and  $\theta_{\text{R}}$ , and (c) three phase parameters,  $\Delta t_{1,\text{R}}$ ,  $\Delta t_{1,\text{NR}}$ , and  $\theta$ , are used. The projections of the real part of the absorptive spectrum along with the pump–probe spectrum are also shown in Fig. 4 below the corresponding 2D spectra. Comparing the different methods, the diagonal peaks are shifted from the diagonal by  $\sim 10$  nm when our previous method of phasing is used. When our new phasing procedure is applied, the diagonal peaks lie along the diagonal and we observe more negative contributions to the 2D spectrum, which is consistent with previous 2DES studies on laser dyes [32,39]. According to the projection slice theorem, a truly absorptive line shape is obtained when the projection of the real part of the absorptive spectrum onto the  $\omega_3$  axis matches that of the pump–probe spectrum taken under the same experimental conditions [31,32]. As can be seen from Fig. 4, our new phasing procedure qualitatively reproduces the pump–probe spectrum when compared to the previous phasing method. The inability to quantitatively reproduce the pump–probe spectrum is attributed to differences in the experimental conditions. When comparing the spectra obtained using two and three phase parameters, we observe a difference in the amplitude of the peaks in the spectra, but the spectra are qualitatively the same.

To further compare the different phasing methods we have also plotted the values of the fitness function obtained for different phasing scenarios. Figure 4d compares our new phasing method to the previous phasing method [4] (pink); we see that the fitness values,  $f$  in eq. 5, decrease by  $\sim 70$  when the new procedure is applied. Figure 4e compares the fitness values obtained from applying the new phasing procedure. There are two main drawbacks to using the projection slice theorem for phasing the spectra. The first is that the intensity of the pump–probe signal can be much weaker than the corresponding 2D spectrum obtained in the background-free geometry [40,41]. The second is that for different phase matching conditions, such as that used for 2D electronic double-quantum coherence spectroscopy, a corresponding pump–probe spectrum cannot be obtained [39,42]. For these scenarios it would be desirable to apply the phasing parameters obtained from an auxiliary dye measurement to the spectra to obtain truly absorptive line shapes. In order to explore the validity of this approach, in Fig. 4e we have plotted the fitness values obtained from phasing each spectra with the corresponding pump–probe spectra [using two phase parameters,  $\theta_{\text{NR}}$  and  $\theta_{\text{R}}$ , (blue) and three phasing parameters,  $\Delta t_{1,\text{R}}$ ,  $\Delta t_{1,\text{NR}}$ , and  $\theta$ , (red)] along with the fitness values obtained from applying the phase determined from applying the

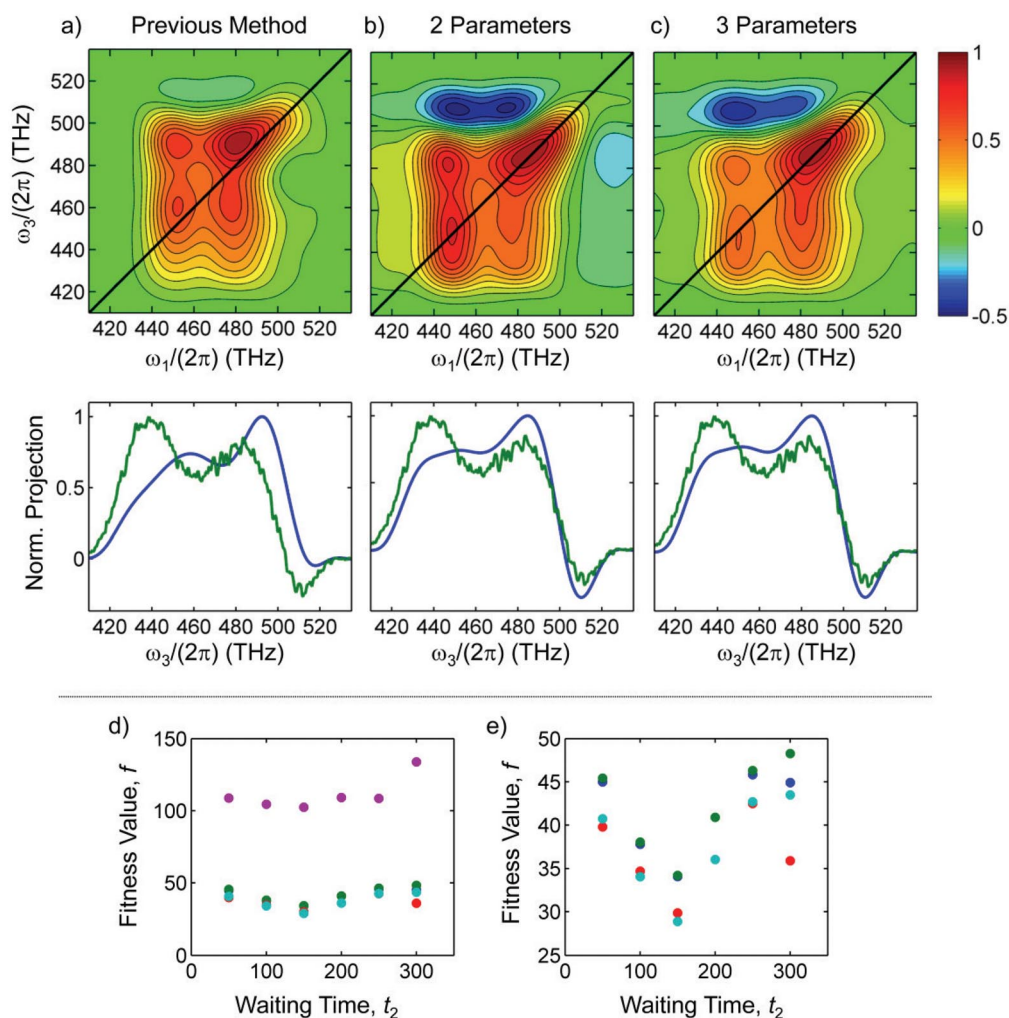


**Fig. 4** The absorptive spectra obtained from our previous method of phasing (a) and applying our current method of phasing using two phase parameters (b) and three phase parameters (c). The corresponding pump–probe spectrum and projection of the absorptive spectrum onto the  $\omega_3$  axis are also shown. The fitness values obtained from phasing spectra at different waiting times are shown in (d) and (e). The color code follows: previous phasing method (pink), two phasing parameters with procedure applied at each  $t_2$  time (blue), two phasing parameters determined from a single  $t_2$  time (green), three phasing parameters with procedure applied at each  $t_2$  time (red), three phasing parameters determined from a single  $t_2$  time (cyan).

phasing procedure to the spectra at  $t_2 = 200$  fs [using two phasing parameters (green) and three phasing parameters (cyan)]. To summarize Fig. 4e, when three parameters are used for phasing, we obtain a slightly better fitness value compared to when three parameters are used, but the standard deviation among the phasing parameters is slightly larger. When we compare the fitness values obtained from applying the phasing procedure at every  $t_2$  point to those obtained from applying the phase determined from a single  $t_2$  point we see the mean fitness value only differs by 1. We attribute this to the phase stability of the experimental set-up [4]. To explore this further, we have applied the phase parameters obtained from the pump–probe spectrum of a different molecular system, in a different sample cell, but otherwise under the same experimental conditions. We find when the phase parameters determined



from the dye measurements are applied to obtain an absorptive spectrum, that the fitness value only varies by  $\sim 4$  when compared to the fitness value obtained from phasing every  $t_2$  point with the corresponding pump–probe spectrum. These results demonstrate that the phase parameters obtained from an auxiliary measurement can be applied to phase other spectra taken under the same experimental conditions.

## EXAMPLES OF 2DES

In this section we demonstrate the ability of 2DES to obtain detailed information on energy transfer and dynamics from the analysis of cross-peaks in the aggregated P3HT and from the analysis of line shapes in PSI. P3HT is a conjugated polymer commonly used as a light harvester and hole conductor in organic photovoltaic devices [43]. PSI is one of the primary pigment–protein complexes that catalyzes oxygenic photosynthesis in plants, algae, and cyanobacteria [44]. Though the systems are very different, understanding the photoinitiated dynamics and processes in these systems may lead to insight into the design of solar cells and solar fuels [45–47].

### P3HT aggregates

The cartoon in Fig. 5a displays the molecular structure of P3HT aggregates. As a semicrystalline macromolecule, P3HT forms  $\pi$ – $\pi$  stacking lamellar structures with a distance  $\sim 3.8$  Å in aggregates or

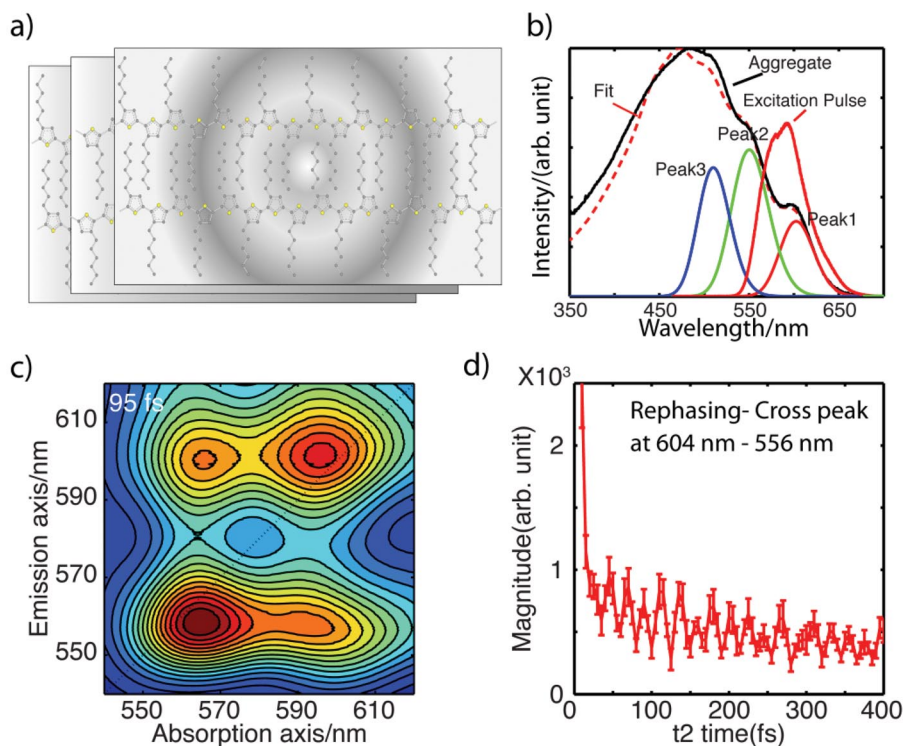


**Fig. 5** (a) Cartoon illustration of P3HT aggregates. (b) Experimental linear absorption spectrum (black) and the corresponding Gaussian fit (dashed-red) are shown with the first three vibronic peaks shown in blue, green, and red along with the spectrum of the incoming laser pulse (red) (c) A representative 2D electronic spectrum of P3HT aggregates at  $t_2 = 95$  fs is shown. (d) The waiting-time-dependent cross-peak amplitude at  $\omega_1 = 556$  nm,  $\omega_3 = 604$  nm for rephasing spectra is shown.



films [48]. The linear absorption spectrum of P3HT aggregates in solution along with the spectrum of the incoming laser pulse is displayed in Fig. 5b. The absorption spectrum is a combination of aggregates in the crystalline domain and single chains in the disordered domain. Three resolved shoulders are assigned to the vibrational progression of the carbon–carbon stretching mode [49]. The line shapes of three vibrational peaks were obtained from fitting the spectrum to Gaussian functions and are labeled peaks 1, 2, and 3 in Fig. 5b. In our 2DES studies, we focus on exploring the ultrafast dynamics of the first two vibronic states, and here we highlight some of the advantages of using 2DES.

One representative 2DES at  $t_2 = 95$  fs is presented in Fig. 5c. The equivalent pump–probe spectrum can be obtained by integrating along the excitation axis. In the pump–probe spectrum, we would observe two peaks while in the 2D spectrum there are four resolvable peaks. In the 2D spectrum, the peaks along the diagonal correspond to the peaks in the linear spectrum, and the cross-peaks indicate that the corresponding diagonal peaks have a common ground state. To further demonstrate the information that can be extracted from the 2D spectrum, in Fig. 5d the waiting-time-dependent trace of the cross-peak at  $\lambda_1 = 604$  nm,  $\lambda_3 = 556$  nm is displayed. We see that the cross-peak oscillates as a function of waiting time. Fourier transformation along the  $t_2$  axis results in an intense peak at 43 THz ( $1432\text{ cm}^{-1}$ ). This frequency corresponds to the difference in energy between the two vibronic transitions at 604 nm ( $16556\text{ cm}^{-1}$ ) and 556 nm ( $17986\text{ cm}^{-1}$ ), indicating that this oscillation arises from a coherence created between the two vibronic states giving rise to peaks 1 and 2. Applying 2DES to P3HT aggregates, we demonstrate the fact that in 2D optical spectroscopy if two transitions having a common ground state lie within the bandwidth of the incoming laser pulse, cross-peaks will be present at early waiting times. Monitoring the waiting-time dependence of these cross-peaks can lead to information pertaining to vibrational coherences in the excited electronic state, which may lead to further insight into the role vibrational motion plays in photochemical and photophysical events.

### PSI of the cyanobacterium *T. elongatus*

PSI is one of the two main pigment–protein complexes that catalyzes oxygenic photosynthesis in plants, algae, and cyanobacteria, via a light-driven electron-transfer reaction [44]. The energy of the absorbed photon is funneled to the reaction center where subsequent charge separation occurs, resulting in a transmembrane electron-transfer reaction. In fact, PSI can be thought of as a molecular-level photovoltaic device, and understanding the pathways and timescales of energy transfer in this system may lead to insight in development of solar cells and production of solar fuels [45,46].

The crystal structure of the trimeric form of PSI from the cyanobacterium *T. elongatus* is shown in Fig. 6 [50]. The trimeric form of PSI contains ~300 chlorophyll molecules shown in green. The chlorophyll molecules are involved in the primary events of photosynthesis, with the antenna chlorophyll harvesting solar energy over a wide spectral range and transferring this energy to the reaction center. The linear absorption spectrum of PSI trimers from *T. elongatus* is shown in Fig. 6. The  $Q_y$  transition associated with the chlorophyll molecules peaks at ~680 nm and is indicated in the spectrum. The  $Q_y$  transition is heterogeneously broadened due to pigment–protein and pigment–pigment interactions. Previous time-resolved studies have gained insight on the mechanism of energy transfer in PSI [51–56], but due to spectral congestion, extracting dynamic and mechanistic information from the  $Q_y$  band is not trivial. 2DES has proven a powerful tool to elucidate energy-transfer dynamics in photosynthetic pigment–protein complexes [16] including FMO [7,57,58], LHCII [59,60], phycobiliproteins [6,61], LH2 [62], LH3 [63], and the reaction center of PSII [64]. Here we summarize our recent results obtained from applying 2DES to PSI [65].

Using 2DES, we observed direct evidence of downhill energy equilibration among the chlorophyll molecules contributing to the  $Q_y$  transition in PSI trimers. Figure 6 displays two 2D spectra at different waiting times,  $t_2 = 60$  fs and  $t_2 = 240$  fs. At early waiting times, the peak is elongated along the diagonal. As  $t_2$  increases, the line shape of the peak evolves, with the amplitude of the peak below the diagonal increasing. This asymmetric evolution of the line shape indicates downhill energy transfer

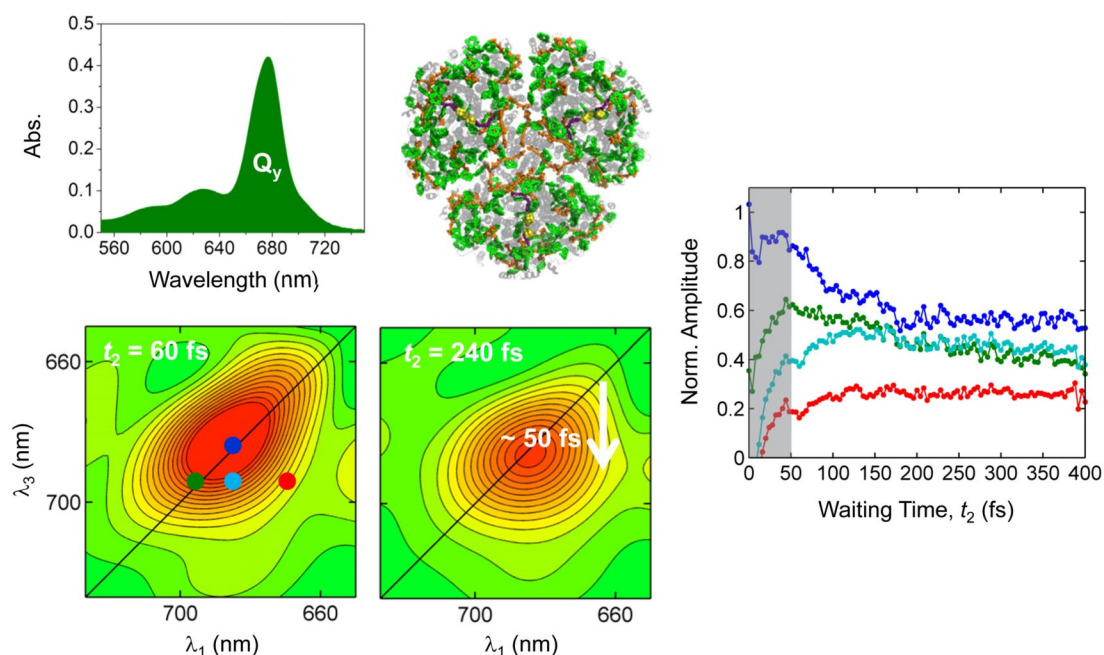


**Fig. 6** The crystal structure (PDB code 4FE1) and linear spectrum of PSI trimers from *T. elongatus* are shown along with corresponding 2D spectra at  $t_2 = 60$  and  $t_2 = 240$  fs. The waiting-time-dependent amplitudes for the points indicated in the 2D spectrum are also shown. This figure has been adapted from ref. [65].

from the higher-lying to the lower-lying states. To obtain further information on the timescale of this energy-transfer process, waiting-time-dependent traces were taken at different points in the spectra (indicated in Fig. 6). From the traces we observe a decay in the diagonal traces, while the off-diagonal traces grow on the  $\sim 50$  fs timescale. Previous studies using transient absorption and fluorescence upconversion experimental techniques were able to obtain detailed mechanistic and dynamic information on PSI; however, these techniques were not able to resolve this ultrafast  $\sim 50$  fs component [53,56,66–77]. Using 2DES, which has both high frequency and time resolution, we directly observe this ultrafast component as a change in the spectral line shape of the peak, demonstrating the remarkable ability to 2DES to map energy flow in complex condensed-phase systems.

## CONCLUSIONS

2DES offers a means by which mechanistic information regarding photochemical and photophysical processes can be mapped out. Since the excitation and detection axes are correlated, pathways of energy flow between different spectroscopic reporters can be directly observed, and information on coupling and electronic structure can also be obtained from the cross-peaks. Here we have given a detailed description of our data processing procedure, demonstrating how to obtain absorptive spectra from raw data. For systems having a weak pump–probe signal, or for systems where the projection slice theorem cannot be applied, we have demonstrated that truly absorptive spectra can be obtained from applying phase parameters determined from auxiliary measurements. To demonstrate the ability of 2DES to gain insight into photophysical events, we have presented two examples. Applying 2DES to aggregates of the conjugated polymer P3HT, we demonstrate that 2DES can be used to gain insight into excited-state vibrational coherences, which in turn may lead to a further understanding of how vibrational motion is coupled to photophysical and photochemical events. Applying 2DES to PSI, we demonstrated the abil-

ity of 2DES to directly observe energy-transfer dynamics on the ultrafast timescale (~50 fs) with both high frequency and time resolution.

## ACKNOWLEDGMENTS

This work was supported by DARPA under the QuBE program, the United States Air Force Office of Scientific Research (FA9550-10-1-0260), and the Natural Sciences and Engineering Research Council of Canada

## REFERENCES

1. V. Butkus, D. Zigmantas, L. Valkunas, D. Abramavicius. *Chem. Phys. Lett.* **545**, 40 (2012).
2. G. Panitchayangkoon, D. V. Voronine, D. Abramavicius, J. R. Caram, N. H. C. Lewis, S. Mukamel, G. S. Engel. *Proc. Natl. Acad. Sci., USA* **108**, 20908 (2011).
3. G. S. Schlau-Cohen, A. Ishizaki, G. R. Fleming. *Chem. Phys.* **386**, 1 (2011).
4. D. B. Turner, K. E. Wilk, P. M. G. Curmi, G. D. Scholes. *J. Phys. Chem. Lett.* **2**, 1904 (2011).
5. J. Yuen-Zhou, J. J. Krich, A. Aspuru-Guzik. *J. Chem. Phys.* **136**, 234501 (2012).
6. E. Collini, C. Y. Wong, K. E. Wilk, P. M. G. Curmi, P. Brumer, G. D. Scholes. *Nature* **463**, 644 (2010).
7. G. Engel, T. Calhoun, E. Read, T. Ahn, T. Mancal, Y. Cheng, R. Blankenship, G. Fleming. *Nature* **446**, 782 (2007).
8. D. R. James, Y. S. Liu, P. Demayo, W. R. Ware. *Chem. Phys. Lett.* **120**, 460 (1985).
9. D. R. James, W. R. Ware. *Chem. Phys. Lett.* **120**, 455 (1985).
10. K. Sahu, S. J. Kern, M. A. Berg. *J. Phys. Chem. A* **115**, 7984 (2011).
11. E. van Veldhoven, C. Khurmi, X. Z. Zhang, M. A. Berg. *ChemPhysChem* **8**, 1761 (2007).
12. S. Mukamel. *Principles of Nonlinear Optical Spectroscopy*, Oxford University Press, New York (1995).
13. S. Mukamel. *Annu. Rev. Phys. Chem.* **51**, 691 (2000).
14. T. H. Joo, Y. W. Jia, J. Y. Yu, M. J. Lang, G. R. Fleming. *J. Chem. Phys.* **104**, 6089 (1996).
15. G. Cerullo, C. Manzoni, L. Luer, D. Polli. *Photochem. Photobiol. Sci.* **6**, 135 (2007).
16. M. Cho. *Chem. Rev.* **108**, 1331 (2008).
17. D. Jonas. *Annu. Rev. Phys. Chem.* **54**, 425 (2003).
18. P. Hamm, M. Zanni. *Concepts and Methods of 2D Infrared Spectroscopy*, Cambridge University Press, New York (2011).
19. M. Cho. *Two-Dimensional Optical Spectroscopy*, CRC Press, Boca Raton (2009).
20. T. Wilhelm, J. Piel, E. Riedle. *Opt. Lett.* **22**, 1494 (1997).
21. S. Akturk, X. Gu, M. Kimmel, R. Trebino. *Opt. Express* **14**, 10101 (2006).
22. R. L. Fork, C. H. B. Cruz, P. C. Becker, C. V. Shank. *Opt. Lett.* **12**, 483 (1987).
23. R. Trebino, K. W. DeLong, D. N. Fittinghoff, J. N. Sweetser, M. A. Krumbugel, B. A. Richman, D. J. Kane. *Rev. Sci. Instrum.* **68**, 3277 (1997).
24. A. Nemeth, J. Sperling, J. Hauer, H. F. Kauffmann, F. Milota. *Opt. Lett.* **34**, 3301 (2009).
25. T. Brixner, T. Mancal, I. V. Stiopkin, G. R. Fleming. *J. Chem. Phys.* **121**, 4221 (2004).
26. S. Gallagher, A. Albrecht, T. Hybl, B. Landin, B. Rajaram, D. Jonas. *J. Opt. Soc. Am. B* **15**, 2338 (1998).
27. J. Hybl, A. Albrecht, S. Faeder, D. Jonas. *Chem. Phys. Lett.* **297**, 307 (1998).
28. L. Lepetit, G. Cheriaux, M. Joffre. *J. Opt. Soc. Am. B* **12**, 2467 (1995).
29. L. Lepetit, M. Joffre. *Opt. Lett.* **21**, 564 (1996).
30. C. Dorrer, N. Belabas, J. Likforman, L. Joffre. *Appl. Phys. B* **70**, S99 (2000).
31. M. Khalil, N. Demirdoven, A. Tokmakoff. *Phys. Rev. Lett.* **90**, 047401 (2003).
32. J. D. Hybl, A. A. Ferro, D. M. Jonas. *J. Chem. Phys.* **115**, 6606 (2001).

33. L. DeFlores, R. Nicodemus, A. Tokmakoff. *Opt. Lett.* **32**, 2966 (2007).
34. A. D. Bristow, D. Karauskaj, X. C. Dai, S. T. Cundiff. *Opt. Express* **16**, 18017 (2008).
35. E. Backus, S. Garrett-Roe, P. Hamm. *Opt. Lett.* **33**, 2665 (2008).
36. S. H. Shim, D. B. Strasfeld, Y. L. Ling, M. T. Zanni. *Proc. Natl. Acad. Sci. USA* **104**, 14197 (2007).
37. S. Park, K. Kwak, M. Fayer. *Laser Phys. Lett.* **4**, 704 (2007).
38. J. M. Anna, M. J. Nee, C. R. Baiz, R. McCanne, K. J. Kubarych. *J. Opt. Soc. Am. B* **27**, 382 (2010).
39. A. Nemeth, F. Milota, T. Mancal, T. Pullerits, J. Sperling, J. Hauer, H. F. Kauffmann, N. Christensson. *J. Chem. Phys.* **133**, 094505 (2010).
40. W. Xiong, M. T. Zanni. *Opt. Lett.* **33**, 1371 (2008).
41. J. A. Myers, K. L. M. Lewis, P. F. Tekavec, J. P. Ogilvie. *Opt. Express* **16**, 17420 (2008).
42. J. Kim, V. M. Huxter, C. Curutchet, G. D. Scholes. *J. Phys. Chem. A* **113**, 12122 (2009).
43. W. Zhang, R. Hu, D. Li, M.-M. Huo, X.-C. Ai, J.-P. Zhang. *J. Phys. Chem. C* **116**, 4298 (2012).
44. R. E. Blankenship. *Molecular Mechanisms of Photosynthesis*, Blackwell Science, Malden, MA (2002).
45. G. D. Scholes, G. R. Fleming, A. Olaya-Castro, R. van Grondelle. *Nat. Chem.* **3**, 763 (2011).
46. R. E. Blankenship, D. M. Tiede, J. Barber, G. W. Brudvig, G. Fleming, M. Ghirardi, M. R. Gunner, W. Junge, D. M. Kramer, A. Melis, T. A. Moore, C. C. Moser, D. G. Nocera, A. J. Nozik, D. R. Ort, W. W. Parson, R. C. Prince, R. T. Sayre. *Science* **332**, 805 (2011).
47. D. Minh Trung, L. Hirsch, G. Wantz. *Adv. Mater.* **23**, 3597 (2011).
48. M. Brinkmann. *J. Polym. Sci.* **49**, 1218 (2011).
49. J. Clark, C. Silva, R. H. Friend, F. C. Spano. *Phys. Rev. Lett.* **98**, 20646 (2007).
50. A. T. Brunger, P. D. Adams, P. Fromme, R. Fromme, M. Levitt, G. F. Schröder. *Structure* **20**, 957 (2012).
51. K. Brettel. *BBA-Bioenergetics* **1318**, 322 (1997).
52. B. Gobets, R. van Grondelle. *BBA-Bioenergetics* **1507**, 80 (2001).
53. A. R. Holzwarth, G. Schatz, H. Brock, E. Bittersmann. *Biophys. J.* **64**, 1813 (1993).
54. A. N. Melkozernov. *Photosynth. Res.* **70**, 129 (2001).
55. S. Savikhin. *Ultrafast Optical Spectroscopy of Photosystem I*, J. H. Golbeck (Ed.), pp. 155–175, Springer, Netherlands (2006).
56. R. van Grondelle, J. P. Dekker, T. Gillbro, V. Sundström. *BBA-Bioenergetics* **1187**, 1 (1994).
57. T. Brixner, J. Stenger, H. Vaswani, M. Cho, R. Blankenship, G. Fleming. *Nature* **434**, 625 (2005).
58. G. Panitchayangkoon, D. Hayes, K. A. Fransted, J. R. Caram, E. Harel, J. Z. Wen, R. E. Blankenship, G. S. Engel. *Proc. Natl. Acad. Sci. USA* **107**, 12766 (2010).
59. T. R. Calhoun, N. S. Ginsberg, G. S. Schlau-Cohen, Y. C. Cheng, M. Ballottari, R. Bassi, G. R. Fleming. *J. Phys. Chem. B* **113**, 16291 (2009).
60. G. S. Schlau-Cohen, T. R. Calhoun, N. S. Ginsberg, E. L. Read, M. Ballottari, R. Bassi, R. van Grondelle, G. R. Fleming. *J. Phys. Chem. B* **113**, 15352 (2009).
61. D. B. Turner, R. Dinshaw, K. K. Lee, M. S. Belsley, K. E. Wilk, P. M. G. Curmi, G. D. Scholes. *Phys. Chem. Chem. Phys.* **14**, 4857 (2012).
62. E. Harel, G. S. Engel. *Proc. Natl. Acad. Sci. USA* **109**, 706 (2012).
63. D. Zigmantas, E. L. Read, T. Mancal, T. Brixner, A. T. Gardiner, R. J. Cogdell, G. R. Fleming. *Proc. Natl. Acad. Sci. USA* **103**, 12672 (2006).
64. J. A. Myers, K. L. M. Lewis, F. D. Fuller, P. F. Tekavec, C. F. Yocum, J. P. Ogilvie. *J. Phys. Chem. Lett.* **1**, 2774 (2010).
65. J. M. Anna, E. E. Ostroumov, K. Maghlaoui, J. Barber, G. D. Scholes. *J. Phys. Chem. Lett.* **3**, 3677 (2012).
66. A. N. Melkozernov, J. Barber, R. E. Blankenship. *Biochemistry* **45**, 331 (2006).
67. A. N. Melkozernov, S. Lin, R. E. Blankenship. *Biochemistry* **39**, 1489 (2000).

68. G. Hastings, S. Hoshina, A. N. Webber, R. E. Blankenship. *Biochemistry* **34**, 15512 (1995).
69. S. Kumazaki, I. Ikegami, H. Furusawa, S. Yasuda, K. Yoshihara. *J. Phys. Chem. B* **105**, 1093 (2001).
70. S. Kumazaki, I. Ikegami, H. Furusawa, K. Yoshihara. *J. Phys. Chem. A* **107**, 3228 (2003).
71. G. R. Fleming, R. van Grondelle. *Curr. Opin. Struct. Biol.* **7**, 738 (1997).
72. M. Du, X. L. Xie, Y. W. Jia, L. Mets, G. R. Fleming. *Chem. Phys. Lett.* **201**, 535 (1993).
73. A. N. Melkozernov, S. Lin, R. E. Blankenship. *J. Phys. Chem. B* **104**, 1651 (2000).
74. M. G. Müller, J. Niklas, W. Lubitz, A. R. Holzwarth. *Biophys. J.* **85**, 3899 (2003).
75. M. G. Müller, C. Slavov, R. Luthra, K. E. Redding, A. R. Holzwarth. *Proc. Natl. Acad. Sci. USA* **107**, 4123 (2010).
76. S. Savikhin, W. Xu, P. R. Chitnis, W. S. Struve. *Biophys. J.* **79**, 1573 (2000).
77. J. T. M. Kennis, B. Gobets, I. H. M. van Stokkum, J. P. Dekker, R. van Grondelle, G. R. Fleming. *J. Phys. Chem. B* **105**, 4485 (2001).